# MULTIDIMENSIONAL OPEN SYSTEM FOR VALVELESS PUMPING

Eunok Jung, Do Wan Kim, Jonggul Lee, and Wanho Lee

Abstract. In this study, we present a multidimensional open system for valveless pumping (VP). This system consists of an elastic tube connected to two open tanks filled with a fluid under gravity. The two-dimensional elastic tube model is constructed based on the immersed boundary method, and the tank model is governed by a system of ordinary differential equations based on the work-energy principle. The flows into and out of the elastic tube are modeled in terms of the source/sink patches inside the tube. The fluid dynamics of this system is generated by the periodic compress-and-release action applied to an asymmetric region of the elastic tube. We have developed an algorithm to couple these partial differential equations and ordinary differential equations using the pressure-flow relationship and the linearity of the discretized Navier-Stokes equations. We have observed the most important feature of VP, namely, the existence of a unidirectional net flow in the system. Our computations are focused on the factors that strongly influence the occurrence of unidirectional flows, for example, the frequency, compression duration, and location of pumping. Based on these investigations, some case studies are performed to observe the details of the flow features.

## 1. Introduction

The phenomenon of a unidirectional net flow driven by pumping without valves is generally called as *valveless pumping* (VP) or *Liebau's effect*. The mechanism of VP has been explained in either a closed-loop tubing system or an open tank system connected by an elastic tube. In both cases, the fluid-structure (elastic tube) interaction by periodic pumping applied to an

asymmetric location of the elastic tube apparently causes a unidirectional flow. In the 1950s, Liebau first studied VP in closed and open systems to explain the mechanism of heart circulation [19, 20, 21]. Many previous studies on VP have reported that there exists not only the interesting fluid dynamics of VP itself but also an efficient and controllable pump mechanism for VP. For instance, a VP system can generate an efficient net flow by controlling the parameters related to the driving force or tube materials. Therefore, VP has been studied extensively through experiments [10, 19, 20, 21, 34], analytical theories [1, 26, 32, 36], and mathematical models [3, 4, 11, 12, 14, 15, 17, 22, 24, 26, 35, 37].

To utilize VP, its controllability is of importance. Unfortunately, it is not yet apparent why a unidirectional net flow exists in VP systems; this flow is believed to be closely related to factors such as the external excitation frequency, elastic wave on the tube, fluid pressure wave, and their correlations. Experiments as well as both simplified modeling and flow simulation with fluid-structure interaction are essential for determining the underlying physics of a valveless flow system. Ottesen [26] reported that the net flow inside a closed elastic loop changes its direction owing to the enforced pumping frequency using a one-dimensional model derived from the Navier-Stokes equations under some assumptions of flow motions. Manopoulos et al. [24] derived a nonlinear one-dimensional hyperbolic partial differential equation (PDE) to consider the flow separation hydraulic losses at the divergent part of the stenosis in the excitation region. Bringley et al. [4], in an interesting study, focused on comparing the results of model with experiments. They introduced an evolutionary quantity to establish a relation with the flow direction observed by Liebau. Borzi and Propst [3] showed that the nonlinearity of the open tank system is not the main factor responsible for the occurrence of the Liebau effect using the accurate computation of a mathematically modified model. Auerbach et al. [1] attempted to introduce a Liebau number that may explain the Liebau effect through an analytic approach in their simplified model of an asymmetric flat pipe derived from the Euler equation. Most recently, Timmermann and Ottesen [37] modeled an open tank system by using the nonstationary Bernoulli principle along a streamline in the tank. They added a marked explanation to the mechanism of valveless flow in an open tank system by introducing horizontal slope frequencies. Although the simplified model reveals physics from VP systems, it differs considerably from the real flow pattern, and therefore, there must be some limitations.

On the other hand, according to the facts reported in [11, 15, 17], in which the full Navier-Stokes models were employed, a valveless flow is known to be strongly affected by the manner in which the elastic tube and the fluid in it interact. This implies that one cannot expect to understand the occurrence of valveless net flow clearly until the interacting flow field in the elastic tube is calculated. Inspired by this viewpoint, we develop a multidimensional fluid-structure model for an open system of VP flow. To calculate the incompressible Navier-Stokes flow (PDE model) interacting with the elastic tube, we employ a

volume-conserved immersed boundary (IB) method. In fact, we have successfully applied this IB method to a couple of valveless flow problems of interest [15, 17]. Because the fluid levels in the two tanks in our open system are moving upwards and downwards, it is very difficult to calculate the detailed flow with the full PDE model of the Navier-Stokes equations. Therefore, the flow in rigid tanks is modeled as the motion of the entire fluid parcel contained in each tank. Using the work-energy principle, a system of ordinary differential equations (ODEs) can be derived for the tank model. In this study, we combine these two physical models using the relationship between the flux and the pressure. First, small source/sink regions called patches are introduced in the flow inside the tube. These regions are viewed as junctions to the tanks. The flux passing through these regions is derived from the energy principle of the fluid parcels in tanks; furthermore, the pressure on these regions can be calculated from the Navier-Stokes equations associated with the source/sink. This type of bridging method has been developed recently by Jung et al. for heart simulations [16]. Modeling the pressure-flux relationship in the source/sink regions becomes the key idea in our bridging approach. The success of this model is attributed to the linear formulation in the fast Fourier transform(FFT) solver for the Navier-Stokes flow. The key advantage of our method in the open tank model lies in simulating the detailed flow bounded by the moving wall of the elastic tube using the full Navier-Stokes equations.

The remainder of this paper is organized as follows. In Section 2, the multidimensional open VP model is introduced: Subsections 2.1 and 2.2 respectively describe the Navier-Stokes flow model associated with the flow in the moving elastic tube (PDE model) and the two-tank model (ODE model). Section 3 presents the numerical implementations for merging the two models. Section 4 presents and discusses the obtained numerical results. Section 5 presents the summary and conclusions of this study.

## 2. Mathematical model of open VP system

In this section, we present a mathematical model of an open VP system. Our open VP model comprises an elastic tube connected to two open tanks. The elastic tube model and the two-tank model are governed by the incompressible Navier-Stokes equations and the ODEs, respectively. The volume-conserved IB method is used for solving the incompressible Navier-Stokes flow interacting with the elastic tube. The fluid motion is generated by the periodic compress-and-release action that is applied on an asymmetric location of the elastic tube. The flow model inside the tank is derived from the energy principle under gravity.

Fig. 1 shows the initial configuration of the two-dimensional elastic tube model. A rectangular box with a long x-axis serves as the computational domain $\Omega$, and it is filled with a viscous incompressible fluid interacting with the elastic tube in the form of a closed curve $\Gamma$. The elastic tube comprises two
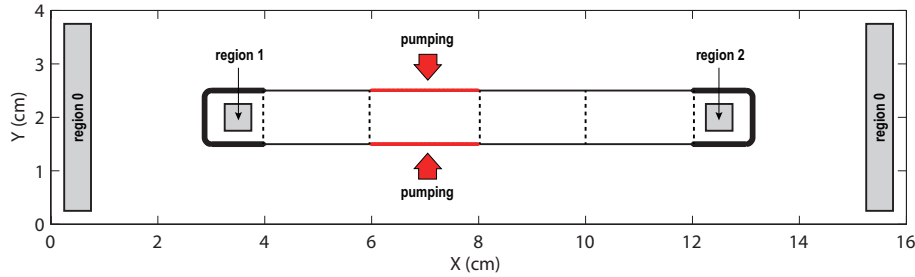
FIGURE 1. The initial configuration of the elastic tube model
immersed in the computational box is shown. Regions 1 and
2 represent the sources/sinks for coupling the elastic tube and
the tank. Region 0 is the exterior source/sink for preserving
the total volume inside the computational domain.

parts with different stiffness: (almost) rigid part (thick curves) and soft part
(thin upper and lower boundaries). There are two source/sink regions inside
the tube to couple the elastic tube and the tank. Because the periodic bound-
ary conditions for the velocity and pressure are imposed on the outer boundary
of the computational domain, the total volume should be conserved in the en-
tire computational box. Therefore, we add the exterior source/sink outside the
tube (region 0). The second quarter of the tube from the left (thick red elastic
tube) is typically chosen as the location of the external pumping source in our
simulations. Note that the open tanks are not visible in this initial configura-
tion, because the tank model is governed by the ODE system. However, two
tanks are virtually attached to regions 1 and 2 by the relationship between the
flux and the pressure.

In Subsection 2.1, we first consider the equations of motion due to the fluid-
structure system that are formulated by the improved volume-conserved IB
method [31]. In Subsection 2.2, based on the energy principle, we describe the
open tank model under gravity.

## 2.1. IB model for tube

In this subsection, we present a mathematical formulation of the equations of
fluid-structure motion using the volume-conserved IB method. The IB method
has been applied to diverse fluid-structure interaction problems in the areas of
biophysics and biomedicine, such as two- and three-dimensional simulations of
blood flow in the heart [8, 27, 28, 29, 30], design of prosthetic cardiac valves
[25], wave propagation in the cochlea [2], VP in a closed loop [11, 12, 14, 15,
17, 22], simulations of whirling instability [23], higher-order IB method [9],
single-cell modeling of tumor dynamics [33], flow of suspensions [7], peristaltic
pumping of solid particles [5], and aquatic animal locomotion [6]. Although
the IB method can be used to deal with sophisticated and time-dependent

materials that interact with the fluid, it has been observed that the volume is not conserved strictly. To reduce the loss of volume during the computation, we employ the volume-conserved IB method in [31].

We describe the mathematical formulation of our PDE system. The fluid velocity, fluid pressure, and fluid force density are denoted by $\mathbf{u}(\mathbf{x}, t)$, $p(\mathbf{x}, t)$, and $\mathbf{f}(\mathbf{x}, t)$ for the space variable $\mathbf{x} = (x, y)$ and time $t$, respectively. The constant fluid density $\rho$ and fluid viscosity $\mu$ are used. The velocity and force density due to the elastic material (tube) are denoted by $\mathbf{U}(s, t)$ and $\mathbf{F}(s, t)$, respectively. The configuration of the elastic material is described in terms of the Lagrangian variable $\mathbf{X}(s, t)$, where the parameter $s$ denotes a material point of the elastic boundary. Then, the governing equations are written as follows:

$$(1) \qquad \rho \left( \frac{\partial \mathbf{u}}{\partial t} + \mathbf{u} \cdot \nabla \mathbf{u} \right) + \nabla p = \mu \nabla^2 \mathbf{u} + \mathbf{f},$$

$$(2) \qquad \nabla \cdot \mathbf{u} = \sum_{j=0}^{2} Q_j(t) \psi_j(\mathbf{x}),$$

$$(3) \qquad \mathbf{f}(\mathbf{x}, t) = \int_\Gamma \mathbf{F}(s, t) \delta(\mathbf{x} - \mathbf{X}(s, t)) \, ds,$$

$$(4) \qquad \frac{\partial \mathbf{X}}{\partial t}(s, t) = \mathbf{U}(\mathbf{X}(s, t), t)$$
$$= \int_\Omega \mathbf{u}(\mathbf{x}, t) \delta(\mathbf{x} - \mathbf{X}(s, t)) \, d\mathbf{x},$$

$$(5) \qquad \mathbf{F}(s, t) = \kappa_t (\mathbf{Z}(s, t) - \mathbf{X}(s, t)) - \frac{\partial E}{\partial \mathbf{X}},$$

$$(6) \qquad E[\mathbf{X}] = \frac{1}{2} \kappa_s \int_\Gamma \left( \left| \frac{\partial \mathbf{X}}{\partial s} \right| - 1 \right)^2 \, ds + \frac{1}{2} \kappa_b \int_\Gamma \left| \frac{\partial^2 \mathbf{X}}{\partial s^2} \right|^2 \, ds.$$

Eqs. (1) and (2) are the viscous incompressible Navier-Stokes equations in Eulerian coordinates; it should be noted that the continuity equation is modified to allow for the source/sink of fluid in the tube. Furthermore, the variable $Q_j(t)$ is introduced for combining this model with the tank model. Actually, by placing fixed source/sink regions (regions 1 and 2) at both ends of the tube by defining the functions $\psi_j$ in (2), the fluid in the two tanks can flow into the tube through these regions and the reverse flow can occur as well. The supports of the source/sink regions are shown in Fig. 1 as shaded squares, region 0. Eqs. (3) and (4) are the interaction equations between the fluid and the elastic tube in the Lagrangian form. A two-dimensional Dirac delta function is present in both equations. In Eq. (3), the fluid force density is obtained by spreading the elastic force density into the fluid using the Dirac delta function. Eq. (4) is the no-slip condition of the viscous fluid. The immersed boundary

moves at the local fluid velocity. Eq. (5) represents the boundary force density as a sum of two terms. The first term provides a force that keeps the elastic boundary positions, $\mathbf{X}(s,t)$, near the given target positions, $\mathbf{Z}(s,t)$. The target position plays a role in maintaining the shape of the tube and applying periodic pumping to the elastic tube. In our model, the same target position as that in [17] is used. The variational derivative of the energy $-\frac{\partial E}{\partial X}$ in the second term of Eq. (5) represents the elastic force density generated by stretching and bending. The parameter $\kappa_t$ is a stiffness constant between the elastic tube and the target positions, and the parameters $\kappa_s$ and $\kappa_b$ are the stiffness and bending coefficients for the elastic boundary, respectively. We use different values of $\kappa_t$ for the (almost) rigid part and the elastic part (see Table 1); however, we use the same value for $\kappa_s$ and $\kappa_b$ for the whole tube.

The spatial distribution of the exterior and interior sources/sinks are specified by nonnegative weight functions $\psi_j(\mathbf{x})$ for $j = 0, 1, 2$, which are bell-shaped on the rectangular support. Each function $\psi_j$ is positive over the corresponding region and zero otherwise, and its integral over the entire fluid domain $\Omega$ is 1: $\int_\Omega \psi_j(\mathbf{x})\, d\mathbf{x} = 1$. The interior weight functions $\psi_1$ and $\psi_2$ of the tube are centered at the locations $(x_1^*, y_1^*) = (3.5, 2)$ and $(x_2^*, y_2^*) = (12.5, 2)$, respectively, and they have a square support with side $a = 0.5$. The interior weight functions are described as follows: for $j=1$ or 2,

$$\psi_j(x,y)$$
$$= \begin{cases} \dfrac{1}{a^2}\left(1 + \cos\left(\dfrac{\pi}{a/2}\bar{x}_j\right)\right)\left(1 + \cos\left(\dfrac{\pi}{a/2}\bar{y}_j\right)\right) & \text{for } (\bar{x}_j, \bar{y}_j) \in [-\frac{a}{2}, \frac{a}{2}]^2, \\ 0 & \text{otherwise,} \end{cases}$$

where $\bar{x}_j = x - x_j^*$ and $\bar{y}_j = y - y_j^*$. The exterior weight function $\psi_0$ has a support in the rectangle, region 0, and it is expressed as follows:

$$\psi_0(x,y)$$
$$= \begin{cases} \dfrac{1}{2M}\displaystyle\sum_{i=1}^{M}\dfrac{1}{a^2}\left(1 + \cos\left(\dfrac{\pi}{a/2}\bar{x}\right)\right)\left(1 + \cos\left(\dfrac{\pi}{a/2}\bar{y}_i\right)\right) & \text{for } (\bar{x}, \bar{y}_i) \in [-\frac{a}{2}, \frac{a}{2}]^2, \\ 0 & \text{otherwise,} \end{cases}$$

where $\bar{x} = x - x^*$, $\bar{y}_i = y - y^* - \Delta y(i-1)$, and $M$ is the number of weight functions to be averaged. The center point $(x^*, y^*)$ to generate the exterior source/sink starts from $(0.5, 0.5)$ and $(15.5, 0.5)$ for the left and right part of the exterior weight functions, respectively. Because we use two exterior sources/sinks near the edges of the domain, the integral of each exterior weight function over the entire fluid domain is $1/2$.

The variable $Q_j(t)\psi_j(\mathbf{x})$, $j = 0, 1, 2$ is the total flux through region $j$ at time $t$, because the integral of $\psi_j(\mathbf{x})$ over the whole fluid domain is 1. A positive and negative value of $Q_j(t)$ represents a source and a sink, respectively. Due to the periodic boundary condition on the computational domain, the total

flux through the exterior sources/sinks is determined by $Q_0 = -(Q_1 + Q_2)$. Therefore, Eq. (2) can be rewritten as

$$(7) \qquad \nabla \cdot \mathbf{u} = \sum_{j=1}^{2} Q_j(t)(\psi_j(\mathbf{x}) - \psi_0(\mathbf{x})).$$

In our multidimensional simulations, the average flow in the PDE tube model is interchanged through the source/sink (regions 1 and 2) to communicate with the ODE tank model. Because the average pressure is the main variable in the tank model, as discussed in the next subsection, we need to calculate the average pressure in regions 1 and 2 from the pressure solution of the IB model (1)–(5) for the interaction between the PDE and the ODE systems.

The average pressure at each region $j$ is defined by

$$(8) \qquad \bar{p}_j = \int_\Omega p(\mathbf{x}, t)\psi_j(\mathbf{x})\, d\mathbf{x}, \qquad j = 0, 1, 2,$$

where $p(\mathbf{x}, t)$ is the fluid pressure of the IB model. Then, the real pressure level in region $j$ can be defined using a reference pressure outside the tube. The average pressure $\bar{p}_0$ at the exterior source/sink is used as a reference pressure in our simulations. The following equation defines the pressure level, $P_j$, in region $j$:

$$(9) \qquad P_j = \bar{p}_j(t) - \bar{p}_0(t) = \int_\Omega p(\mathbf{x}, t)(\psi_j(\mathbf{x}) - \psi_0(\mathbf{x}))\, d\mathbf{x}.$$

The pressure level $P_j$ for $j = 1, 2$ is used for combining the IB model with the tank model in Subsection 2.2.

## 2.2. Energy preserving model for tanks

This subsection describes the open tank model based on the work-energy principle. It should be noted that the fluxes $Q_1(t)$ and $Q_2(t)$ have not yet been determined. To drive the flux interaction equations between the IB tube model and the open tank model, it is important to derive physically meaningful flux conditions at both junctions between the elastic tube and the two tanks. Toward this end, the principle of energy transfer is employed, i.e., the time rate of change in energy (or work) of a lumped fluid in the tank is equivalent to the power done by the surroundings under gravity. Two rigid cuboidal tanks with a square base are attached to regions 1 and 2. The heights of the fluid in the left and the right tank are denoted by $H_1(t)$ and $H_2(t)$, respectively. In the tanks, the inertia force of the fluid is assumed to be dominant enough to ignore the friction force due to viscosity. In addition, the fluid in a tank is assumed to move up and down with the same velocity as if it is a single body, i.e., the velocities of the lump of fluid in the tanks, $v_1(t)$ and $v_2(t)$, are functions of time only for the incompressibility of the fluid. If the internal energy of the fluid is ignored, then the total energy $e_1$ of the fluid in the left tank is the sum

of the kinetic and potential energies, and it is given as follows:

$$(10) \qquad e_1 = \int_0^{H_1(t)} \frac{1}{2}\rho v_1^2(t)a_1\,dy + \int_0^{H_1(t)} \rho gy a_1\,dy,$$

where the parameters $g$ and $a_1$ represent the gravitational constant and the cross-sectional area of the left rigid tank, respectively.

By substituting the relation $Q_1(t) = a_1 v_1(t)$ into the energy Eq. (10), we obtain the following equation:

$$(11) \qquad \begin{aligned} e_1 &= \frac{1}{2}\rho a_1 H_1(t)v_1^2 + \frac{1}{2}\rho g a_1 H_1^2(t) \\ &= \frac{1}{2}\rho Q_1^2(t)\frac{H_1(t)}{a_1} + \frac{1}{2}\rho g a_1 H_1^2(t). \end{aligned}$$

Furthermore, the fluid velocity in the left tank satisfies $v_1(t) = -\dot{H}_1$. Then, the incompressibility leads to the time rate of changes for $e_1$ as follows:

$$(12) \qquad \begin{aligned} \dot{e}_1 &= \rho Q_1(t)\dot{Q}_1(t)\frac{H_1(t)}{a_1} + \frac{1}{2}\rho Q_1^2(t)\frac{\dot{H}_1(t)}{a_1} + \rho g a_1 H_1(t)\dot{H}_1(t) \\ &= \rho Q_1(t)\dot{Q}_1(t)\frac{H_1(t)}{a_1} - \frac{1}{2}\rho Q_1^2(t)\frac{Q_1(t)}{a_1^2} - \rho g Q_1(t)H_1(t). \end{aligned}$$

The sign of the fluid velocity in the tank is set to be positive if the direction of flux is from the tank to the tube for both the left and the right tanks.

On the other hand, the time rate of change for the energy $e_1$ is equal to the work per unit time done by the surrounding air pressure $P^{atm}$ on the top surface of the tank and the pressure level in region 1, i.e.,

$$(13) \qquad \dot{e}_1 = -(P_1(t) + P^{atm})Q_1(t),$$

where $P_1$ is defined at (9). For flux $Q_1(t)$, comparing (12) and (13), we conclude

$$(14) \qquad \dot{Q}_1 = \frac{Q_1^2(t)}{2a_1 H_1(t)} + ga_1 - \frac{a_1}{\rho}\frac{P_1(t) + P^{atm}}{H_1(t)}.$$

Similarly, we can derive the following model for $Q_2(t)$:

$$(15) \qquad \dot{Q}_2 = \frac{Q_2^2(t)}{2a_2 H_2(t)} + ga_2 - \frac{a_2}{\rho}\frac{P_2(t) + P^{atm}}{H_2(t)}.$$

Using the relationship between the flux and the fluid velocity, we can also calculate the time rate of change for the tank height as follows:

$$(16) \qquad \dot{H}_1 = -\frac{1}{a_1}Q_1(t),$$

and

$$(17) \qquad \dot{H}_2 = -\frac{1}{a_2}Q_2(t).$$

Eqs. (14)–(17) are the governing equations for the tank model. In the next section, we discuss how this tank model is coupled to the PDE tube model in the numerical implementation.

## 3. Numerical implementation

This section describes how the PDE tube model and the ODE tank model are merged in the numerical implementation. In our simulations, a first-order volume-conserved IB method is employed for solving the two-dimensional PDE tube (1)–(5), and the Runge-Kutta-Fehlberg method is used for solving the ODE tank model (14)–(17).

The objective is to compute the updated fluid velocity and position, $\mathbf{u}^{n+1}$ and $\mathbf{X}^{n+1}$, respectively, from the given $\mathbf{u}^n$ and $\mathbf{X}^n$. This is done in the following steps:

Step 1. The immersed boundary force density $\mathbf{F}^n$ is obtained by the boundary configuration $\mathbf{X}^n$ and the given target position $\mathbf{Z}^n$.

$$(18) \qquad \mathbf{F}^n = \kappa_t\big(\mathbf{Z}^n - \mathbf{X}^n\big) + \frac{\partial}{\partial s}(T^n \boldsymbol{\tau}^n) - \kappa_b \frac{\partial^4 \mathbf{X}^n}{\partial s^4},$$

where

$$(19) \qquad T^n = \kappa_s\left(\left|\frac{\partial \mathbf{X}^n}{\partial s}\right| - 1\right) \text{ and } \boldsymbol{\tau}^n = \frac{\partial \mathbf{X}^n}{\partial s}\bigg/\left|\frac{\partial \mathbf{X}^n}{\partial s}\right|.$$

Here, $T^n$ is the tension and $\boldsymbol{\tau}^n$, the unit tangent vector. For more detailed descriptions of the stretching and bending force densities, see [18].

Step 2. The fluid force density $\mathbf{f}^n$ is calculated by spreading the boundary force density $\mathbf{F}^n$ into the nearby fluid grid using the discrete $\delta$-function.

$$(20) \qquad \mathbf{f}^n = \sum_s \mathbf{F}^n(s)\delta^2(\mathbf{x} - \mathbf{X}^n(s))\Delta s,$$

where $\delta^2(\mathbf{x})$ is the discretized two-dimensional Dirac delta function, and $\Delta s$ is the distance between boundary points.

Step 3. Consider the discretized version of the Navier-Stokes system (1) and (7) as follows:

$$(21) \quad \begin{cases} \rho\left(\dfrac{\mathbf{u}^{n+1}-\mathbf{u}^n}{\Delta t} + (\mathbf{u}^n \cdot \nabla_h^{\pm})\mathbf{u}^n\right) + \mathbf{D}^0 p^{n+1} = \mu \displaystyle\sum_{\alpha=1,2} D_\alpha^+ D_\alpha^- \mathbf{u}^{n+1} + \mathbf{f}^n, \\[2ex] \mathbf{D}^0 \cdot \mathbf{u}^{n+1} = \displaystyle\sum_{j=1}^{2} Q_j^{n+1}(\psi_j(\mathbf{x}) - \psi_0(\mathbf{x})), \end{cases}$$

where $\mathbf{u}^n \cdot \nabla_h^{\pm} = u^n D_x^{\pm} + v^n D_y^{\pm}$, and $D^{\pm}$ represents the upwind scheme. We use the forward $(D^+)$ and backward $(D^-)$ difference operators in the standard way. For the central difference operator $\mathbf{D}^0$, we employed the volume-conserved operator introduced by [31].

The periodic boundary condition on the computational domain enables us to effectively solve the flow system using FFT. It should be noted that $Q_1^{n+1}$ and $Q_2^{n+1}$ have not yet been determined. These two flow values are obtained by Steps 3.1 and 3.2 as described below.

Step 3.1  This step is more important for solving our multidimensional system. Because the system (21) is linear in the unknown $\mathbf{u}^{n+1}$ and $p^{n+1}$, we can split the system (21) into the following three systems:

$$
(22) \quad
\begin{cases}
\rho\left(\dfrac{\mathbf{u}_f^{n+1}-\mathbf{u}^n}{\Delta t}+(\mathbf{u}^n\cdot\nabla_h^{\pm})\mathbf{u}^n\right)+\mathbf{D}^0 p_f^{n+1}=\mu\displaystyle\sum_{\alpha=1,2}D_\alpha^+ D_\alpha^-\mathbf{u}_f^{n+1}+\mathbf{f}^n, \\[2ex]
\mathbf{D}^0\cdot\mathbf{u}_f^{n+1}=0,
\end{cases}
$$

$$
(23) \quad
\begin{cases}
\rho\dfrac{\mathbf{u}_1^{n+1}}{\Delta t}+\mathbf{D}^0 p_1^{n+1}=\mu\displaystyle\sum_{\alpha=1,2}D_\alpha^+ D_\alpha^-\mathbf{u}_1^{n+1}, \\[2ex]
\mathbf{D}^0\cdot\mathbf{u}_1^{n+1}=\psi_1(\mathbf{x})-\psi_0(\mathbf{x}),
\end{cases}
$$

and

$$
(24) \quad
\begin{cases}
\rho\dfrac{\mathbf{u}_2^{n+1}}{\Delta t}+\mathbf{D}^0 p_2^{n+1}=\mu\displaystyle\sum_{\alpha=1,2}D_\alpha^+ D_\alpha^-\mathbf{u}_2^{n+1}, \\[2ex]
\mathbf{D}^0\cdot\mathbf{u}_2^{n+1}=\psi_2(\mathbf{x})-\psi_0(\mathbf{x}).
\end{cases}
$$

In the first system (22), the full Navier-Stokes equations without the source/sink terms are considered. Because $\mathbf{f}^n$ and $\mathbf{u}^n$ are known values, we can solve the system to update $\mathbf{u}_f^{n+1}$ and $p_f^{n+1}$. Because the second and third systems, (23) and (24), respectively, involve only the given weight functions in the source/sink term, $\psi_j$ for $j=0,1,2$, without the convection and body force terms, we can also update $(\mathbf{u}_1^{n+1},p_1^{n+1})$, and $(\mathbf{u}_2^{n+1},p_2^{n+1})$. Then, using the linearity of (21), the solutions $\mathbf{u}^{n+1}$ and $p^{n+1}$ can be written as follows:

$$(25) \qquad \mathbf{u}^{n+1}=\mathbf{u}_f^{n+1}+Q_1^{n+1}\mathbf{u}_1^{n+1}+Q_2^{n+1}\mathbf{u}_2^{n+1},$$

$$(26) \qquad p^{n+1}=p_f^{n+1}+Q_1^{n+1}p_1^{n+1}+Q_2^{n+1}p_2^{n+1}.$$

Step 3.2  Now, we consider the discretized ODE tank model. We use the Runge-Kutta-Fehlberg method for solving *four* equations, Eqs. (14)–(17). However, the number of unknowns, $Q_i$, $H_i$, and $P_i$ for $i=1,2$, is six. To derive two more equations for pressure, the pressures $P_1$ and $P_2$ in (9) are used:

$$P_1^{n+1}=\sum_{\mathbf{x}}p^{n+1}(\mathbf{x})\big(\psi_1(\mathbf{x})-\psi_0(\mathbf{x})\big)h^2,$$

$$P_2^{n+1}=\sum_{\mathbf{x}}p^{n+1}(\mathbf{x})\big(\psi_2(\mathbf{x})-\psi_0(\mathbf{x})\big)h^2,$$

where $\sum_{\mathbf{x}}$ denotes the sum over the rectangular lattice with the mesh size $h$ in the physical space in which the fluid variables are defined. If we substitute Eq. (26) into the above two equations for $P_1^{n+1}$ and $P_2^{n+1}$, the average pressures in regions 1 and 2 can be simply rewritten as

$$(27) \qquad P_1^{n+1} = c_{10} + c_{11}Q_1^{n+1} + c_{12}Q_2^{n+1},$$

$$(28) \qquad P_2^{n+1} = c_{20} + c_{21}Q_1^{n+1} + c_{22}Q_2^{n+1},$$

where the coefficients are calculated to be

$$c_{10} = \sum_{\mathbf{x}} p_f^{n+1}(\mathbf{x})(\psi_1(\mathbf{x}) - \psi_0(\mathbf{x}))h^2,$$

$$c_{11} = \sum_{\mathbf{x}} p_1^{n+1}(\mathbf{x})(\psi_1(\mathbf{x}) - \psi_0(\mathbf{x}))h^2,$$

$$c_{12} = \sum_{\mathbf{x}} p_2^{n+1}(\mathbf{x})(\psi_1(\mathbf{x}) - \psi_0(\mathbf{x}))h^2,$$

$$c_{20} = \sum_{\mathbf{x}} p_f^{n+1}(\mathbf{x})(\psi_2(\mathbf{x}) - \psi_0(\mathbf{x}))h^2,$$

$$c_{21} = \sum_{\mathbf{x}} p_1^{n+1}(\mathbf{x})(\psi_2(\mathbf{x}) - \psi_0(\mathbf{x}))h^2,$$

$$c_{22} = \sum_{\mathbf{x}} p_2^{n+1}(\mathbf{x})(\psi_2(\mathbf{x}) - \psi_0(\mathbf{x}))h^2.$$

$p_f^{n+1}$, $p_1^{n+1}$, and $p_2^{n+1}$ are obtained from Step 3.1. Consequently, we can solve four ODEs (14)–(17) associated with (27) and (28) for $P_j^{n+1}, Q_j^{n+1}$, and $H_j^{n+1}$ for $j = 1, 2$.

Using the computed values, $Q_1^{n+1}$ and $Q_2^{n+1}$, we can complete Step 3 to compute $\mathbf{u}^{n+1}$ and $p^{n+1}$.

Step 4. The updated fluid velocity $\mathbf{u}^{n+1}$ obtained in Step 3 is interpolated into the old boundary position $\mathbf{X}^n$ by the discrete Dirac delta function. Finally, we can update $\mathbf{X}^{n+1}$ by solving the following:

$$(29) \qquad \mathbf{X}^{n+1}(s) = \mathbf{X}^n(s) + \Delta t \sum_{\mathbf{x}} \mathbf{u}^{n+1}(\mathbf{x})\delta^2(\mathbf{x} - \mathbf{X}^n(s))h^2.$$

## 4. Numerical results and discussion

In this section, we discuss the numerical results of the open VP system. Various fluid motions are produced in the open VP system by applying periodic forcing at an asymmetric location on the elastic tube (see Fig. 1). Tables 1 and 2 respectively show the physical and numerical parameters in CGS units.

In this study, we focus on the main features of VP that have been reported in previous studies of closed or open VP systems: the existence of a unidirectional net flow and the parameter sensitivity of the direction and magnitude of a net flow. Because our system is not closed, a net flow is always zero after the

TABLE 1. Physical parameters.

| Physical parameters | Symbol | Value |
|---|---|---|
| Computational domain | $X_{scale} \times Y_{scale}$ | $16\,cm \times 4\,cm$ |
| Length of tube | $L$ | $10\,cm$ |
| Radius of tube | $r$ | $0.5\,cm$ |
| Initial fluid height in tank | $H_1 = H_2$ | $10\,cm$ |
| Cross-sectional area of tank | $a_1 = a_2$ | $4\,cm^2$ |
| Fluid density | $\rho$ | $1\,g/cm^3$ |
| Gravitational constant | $g$ | $980\,g \cdot cm/s^2$ |
| Fluid viscosity | $\mu$ | $0.01\,g/(cm \cdot s)$ |
| Frequency | $f\ (1/T)$ | $0.5\,Hz \sim 60\,Hz$ |
| Compression duration | $d$ | $0.1 \sim 1$ |
| Amplitude (target) | $A_0$ | $0.6r = 0.3\,cm$ |
| Stiffness (rigid tube) | $\kappa_t$ | $5.0 \times 10^6\,g/(cm \cdot s^2)$ |
| Stiffness (soft tube) | $\kappa_t$ | $5.0 \times 10^5\,g/(cm \cdot s^2)$ |
| Stiffness (stretching) | $\kappa_s$ | $5.0 \times 10^4\,g/s^2$ |
| Stiffness (bending) | $\kappa_b$ | $3.0 \times 10^2\,g \cdot cm/s^2$ |

TABLE 2. Computational parameters.

| Computational parameters | Symbol | Value |
|---|---|---|
| Fluid grid | $N_x \times N_y$ | $512 \times 128$ |
| Number of upper (lower) soft boundary points | $M_{upper} = M_{lower}$ | $1024$ |
| Number of left (right) rigid boundary points | $M_{left} = M_{right}$ | $402$ |
| Mesh width | $h = \Delta x = \Delta y$ | $0.03125\,cm$ |
| Initial distance between boundary points | $\Delta s = h/4$ | $0.0078125\,cm$ |
| Time step | $\Delta t$ | $2.5 \times 10^{-5}\,s$ |
| Simulated time | $t_{max}$ | $1\,s \sim 20\,s$ |

periodic steady-state is reached. We define the flow causing a height difference between the two tanks as *a net directional flow*. The net directional flow, which is measured by the time-averaged height difference from the right to the left tank, has a positive or negative value. A positive value denotes a flow from the left to the right tank, and a negative value denotes a flow in the opposite direction.

We first check the validation of our model and then present parametric studies on the effect of the frequency and compression duration of driving force, and the location and width of pumping. The fluid dynamics in some cases is also investigated.

### 4.1. Validation

We consider two different settings. In the first setting, the same tank width, $2\,cm$, is considered for both tanks; however, the initial fluid levels in the tanks are different. As the initial state, the fluid levels in the left and the right tanks are chosen as $13\,cm$ and $7\,cm$, respectively. In the second setting, different tank widths and fluid levels are considered. The tank widths and fluid levels are $1\,cm$ and $18\,cm$ for the left tank and $2\,cm$ and $8\,cm$ for the right tank, respectively. The simulation duration is $20\,s$, and other parameters are listed in Tables 1 and 2. Figs. 2 and 3 show the fluid heights in both tanks as a function of time for the first and second settings, respectively. As expected, in both settings, oscillatory motions are observed initially, and then, the levels of the left and right tanks reach almost $10\,cm$, which is the equilibrium state. In fact, the fluid levels at the steady-state are not exactly $10\,cm$, because the gravity and elasticity of the tube lead to a little fluid in the tanks seeping into the elastic tube for equilibrium.

Now, we check the numerical accuracy. A convergence test is performed by the solutions computed on three different grid sizes of $N_x \times N_y = 256 \times 64$, $512 \times 128$, and $1024 \times 256$. A subscript of the velocity field denotes the grid size in the $x$ direction. For instance, $u_{256}$ represents the $u$-directional velocity in the grid size of $256 \times 64$. The convergence ratio for the velocity field $(u, v)$ in $L_2$ norm is 1.9014 at $t = 1\,s$ and $f = 10\,Hz$, that is,

$$\frac{\sqrt{\|u_{512} - u_{256}\|_2^2 + \|v_{512} - v_{256}\|_2^2}}{\sqrt{\|u_{1024} - u_{512}\|_2^2 + \|v_{1024} - v_{512}\|_2^2}} = 1.9014.$$

This ratio is close to 2, which implies that the scheme is first-order accurate in time.

### 4.2. Parametric studies

**The time-averaged height differences between two tanks as functions of the frequency and the compression duration of pumping.** We first investigate the impact of the pumping frequency on the open VP model. Fig. 4 shows the time-averaged height differences between two tanks as a function of the pumping frequency. The frequency range is 0.5–60 $Hz$, in which 337 different values are considered, and the compression duration is fixed as $d = 0.5$. Other parameters are listed in Tables 1 and 2. The compression duration is defined by the ratio of the time for compression and relaxation during a period. For example, if the compression duration $d$ is equal to 0.5, then compression is applied for the first half of the period and relaxation, for the rest of the period. Each dot in the figure indicates an individual numerical experiment during the simulated time, 5 $s$. The positive or negative value indicates the existence of a net directional flow. From Fig. 4, it is obvious that VP strongly depends on the pumping frequency, as observed in previous studies [4, 11, 12, 14, 15, 17, 22, 24, 26, 35, 37]. Two positive peaks at around
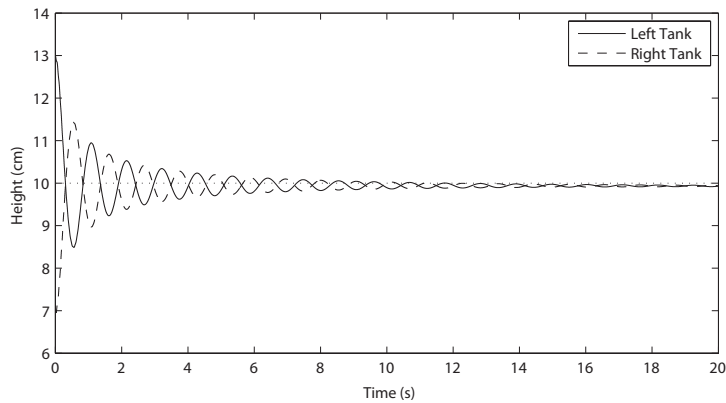
FIGURE 2. The fluid levels in tanks as a function of time are shown. The same tank width, $2\,cm$, is considered; however, different initial height levels are imposed. The left and right tank levels are chosen as $13\,cm$ and $7\,cm$, respectively.
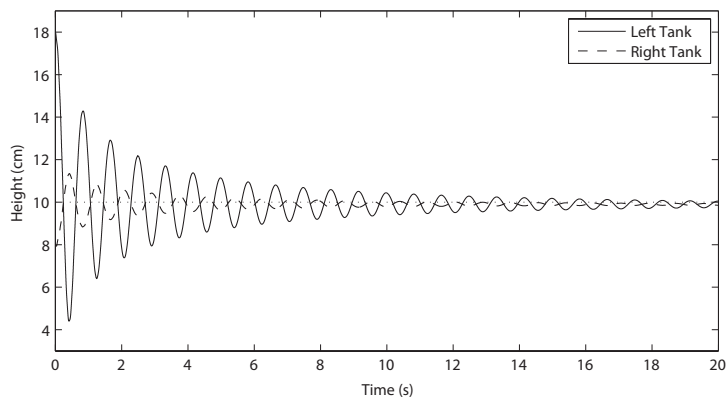


FIGURE 3. The fluid levels in tanks as a function of time are shown. The tank widths and fluid heights are chosen as $1\,cm$ and $18\,cm$ for the left tank and $2\,cm$ and $8\,cm$ for the right tank, respectively.

$f = 16\,Hz$ and $f = 52\,Hz$ and one negative peak at around $f = 33\,Hz$ are observed, implying that the flow direction and level difference are determined by the driving frequency. At most frequencies less than around $14\,Hz$, almost zero flows are observed.

Next, we investigate the effect of the compression duration of pumping on the net directional flow. Fig. 5 shows the time-averaged height differences
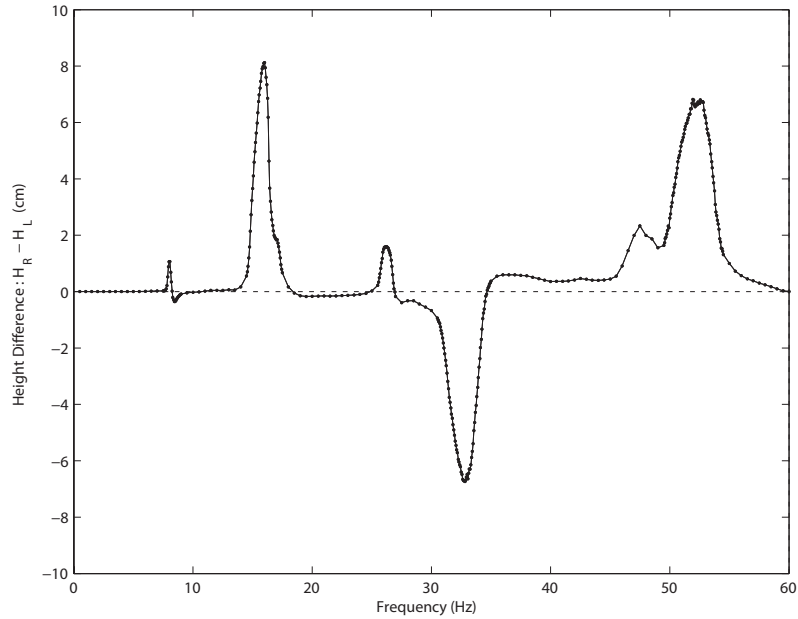
FIGURE 4. The time-averaged height differences between two
tanks as a function of the frequency is shown.

between two tanks as functions of the frequency and the compression dura-
tion. We consider 148 curves for a frequency of 0.05–60 $Hz$ with 10 different
compression durations from 0.1 to 1. The ten curves of the level differences
as a function of the frequency at the fixed compression duration have similar
patterns. However, the magnitude of the level difference is mostly maximized
around intermediate values of the compression duration, and it decreases at ex-
tremes of the compression duration. Overall, it is confirmed that the frequency
and compression duration are critical factors in controlling the VP mechanism.

In Fig. 6, the free vibration of the upper boundary of the tube at the middle
of the pumping region, $x = 7\ cm$, and its Fourier transform with 10,000 sample
points over 1 s is shown in the top and bottom frames, respectively. The
displacement of the observed point as a function of time is generated by the
external pumping over five periods with the pumping frequency $f = 5\ Hz$ and
compression duration $d = 0.5$ and then by vibration without external pumping
for the rest of the simulated time. The Fourier transform in the bottom frame
in Fig. 6 shows a natural frequency at $17\ Hz$ and harmonics at $35\ Hz$ and
$56\ Hz$. As expected, these frequencies approximately coincide with the peak
frequencies shown in Fig. 4, which are $f = 16\ Hz$, $33\ Hz$, and $52\ Hz$.

**Influence of the location and the width of pumping region.** We
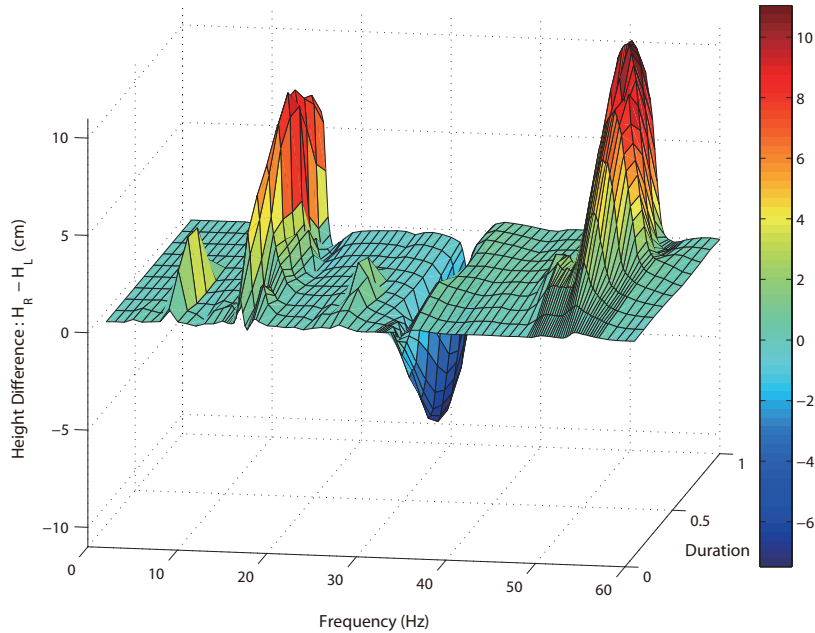investigate the influence of the location and width of the pumping region on

FIGURE 5. The time-averaged height differences between two
tanks as functions of the frequency and the compression dura-
tion are shown.

the open VP system. The parameters are listed in Tables 1 and 2, except
for $d = 0.5$. Pumping is applied to the left part of the elastic tube in all
simulations.

In Fig. 7, first, we consider four different pumping positions with a fixed
length of pumping region, $\frac{1}{8} \times length\ of\ the\ elastic\ part\ of\ the\ tube$. The pump-
ing location is shifted from the left (C0) to the right (C3). Next, in Fig. 8,
we consider three different widths of the pumping region. The widths of the
pumping regions, P1, P2, and P3, are 1 $cm$, 1.5 $cm$, and 2 $cm$, respectively;
however, the center for pumping is fixed in the left one-fourth of the elastic
tube for all three cases. In Fig. 7, at frequencies below 30 $Hz$, almost zero
net directional flows are observed except near a positive peak at $f = 16Hz$ in
all four cases. However, there is no consistency in the curves at frequencies
higher than 30 $Hz$. Timmermann and Ottesen recently reported [37] that the
pumping position does not change the location of the resonance points. This
is because the range of the frequency they considered is below 16 $Hz$. We
also observe that positive net directional flows dominate if pumping is applied
to location C0, which is the left-most end of the elastic tube. This result is
consistent with a previous study [17]. Furthermore, the magnitudes of the level
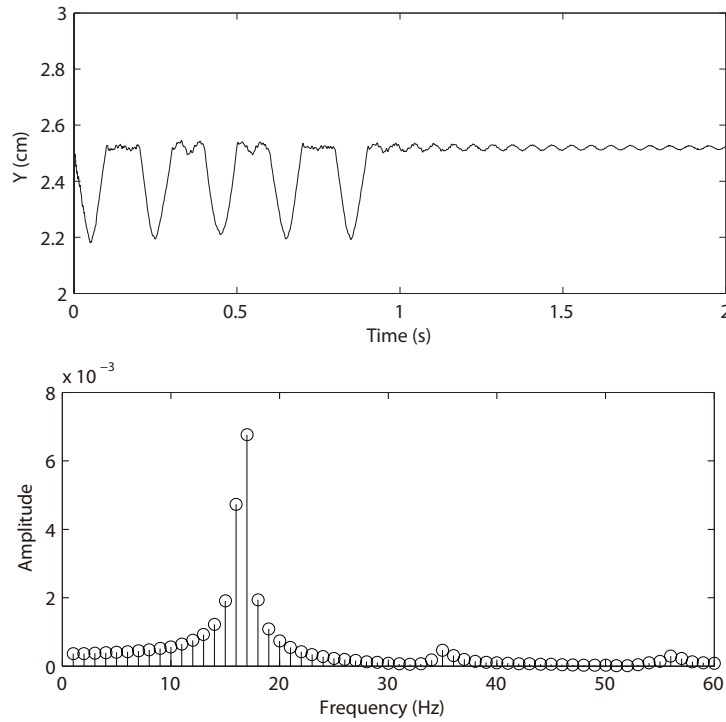difference at most peaks are larger at pumping location C0 than in other cases.

FIGURE 6. Free vibration test at the middle of the pumping region on the upper tube at $f = 5\,Hz$ is shown in the top frame. Its Fourier transform on the bottom frame shows a natural frequency at $17\,Hz$ and harmonics at $35\,Hz$ and $56\,Hz$. Other parameters are listed in Tables 1 and 2.

As the pumping location moves toward the center, as is the case with location C3, the magnitudes of the level difference at most peaks decrease. We need a high frequency to obtain larger level differences, as is the case with location C3. The results shown in Fig. 8 are quite different from those shown in Fig. 7: the three curves have similar patterns except for the magnitude. A larger magnitude is produced as a longer pumping width is applied. The scales of the $y$-axis in Fig. 7 and Fig. 8 are different. Overall, similar features are investigated if the center of pumping is fixed. A large amount of net directional flow is obtained by choosing a long pumping width. If the pumping length is fixed, then an efficient net directional flow can be obtained by controlling the pumping location.
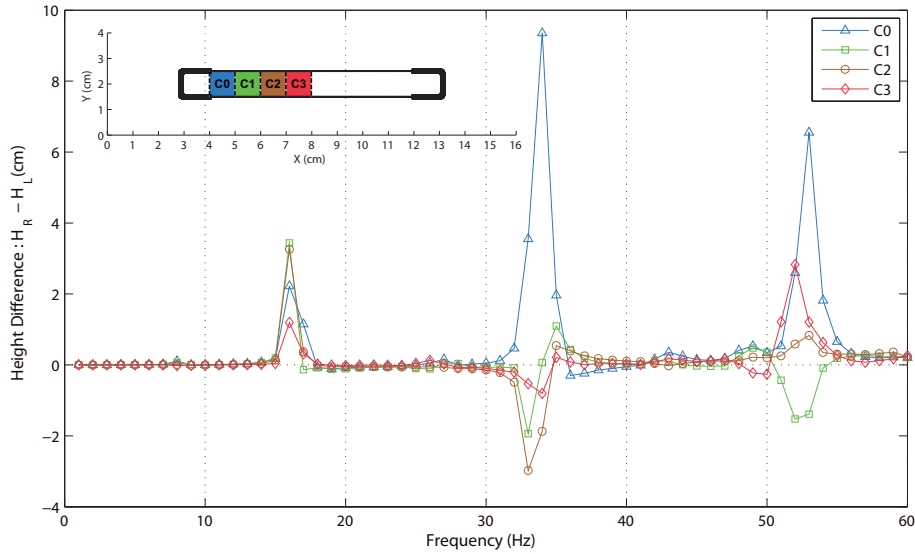
FIGURE 7. The time-averaged height differences between two tanks as a function of the frequency are plotted at four different pumping positions. An initial configuration with four different pumping positions is shown in the top left-hand corner of the figure. The same pumping length is chosen as $\frac{1}{8} \times length$ of the elastic part of the tube.

## 4.3. Case studies

In this subsection, three special cases are considered for studying the motions of fluid dynamics in detail. We chose these cases based on the results shown in Fig. 4: an almost zero, a positive peak, and a negative peak net directional flow. A net directional flow is again measured by the time-averaged height difference between two tanks. We chose the following three cases:

- Positive net directional flow
  $f = 16 \, Hz$ (averaged level difference: $8.066 \, cm$)
- Almost zero net directional flow
  $f = 25 \, Hz$ (averaged level difference: $0.026 \, cm$)
- Negative net directional flow
  $f = 33 \, Hz$ (averaged level difference: $-6.637 \, cm$)

The parameters are the same as those shown in Fig. 4. The fluid motions are driven by the oscillations imposed on the left second quarter of the elastic part of the tube. For all three cases, we investigated the level differences as a function of time to show the nature of oscillations and the net progress of fluid motions. Fig. 9 shows the height differences of the fluid level in two tanks as
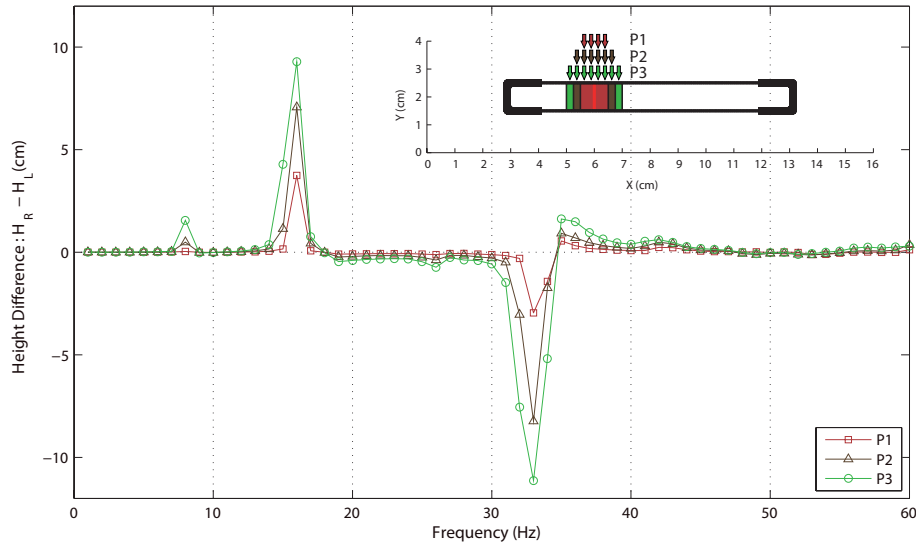
FIGURE 8. The time-averaged height differences between two
tanks as functions of the frequency are plotted at three dif-
ferent widths of the pumping region. An initial configuration
with three different widths of the pumping region is shown in
the top of the figure. The lengths of the regions P1, P2, and
P3 are $1\,cm$, $1.5\,cm$, and $2\,cm$, respectively, with a quarter of
the elastic part of the tube as the center.

a function of time over the simulated time. The positive net directional flow
at $f = 16\,Hz$, almost zero net directional flow at $f = 25\,Hz$, and negative
net directional flow at $f = 33\,Hz$ are considered in the first, second, and third
rows, respectively. The first column shows the height differences between the
two tanks as a function of time over the simulated time $5\ s$. For the detailed
motions of height differences, the last 5 cycles of height differences are shown
in the second column. Fig. 9 clearly shows the existence of net directional flow
in our open tank VP system. Furthermore, we can observe almost periodic
motions of height differences, and the period of the height difference is almost
the same as that of external pumping, $1/f$, in all three cases.

Because we use the IB method for solving the PDE system, the volume
loss is one of the critical issues. In Fig. 10, the volume loss ratios, $(V_{ini} -
V(t))/V_{ini}$, is shown for the cases with pumping frequency $f = 16\,Hz$ (dot),
$25\,Hz$ (solid), and $33\,Hz$ (dash) and the case without pumping (dotted dash)
over the simulation time of $1\ s$. $V_{ini}$ represents the initial volume of the tube.
Fig. 10 shows that the maximum volume loss is around $0.2\,\%$ over the time
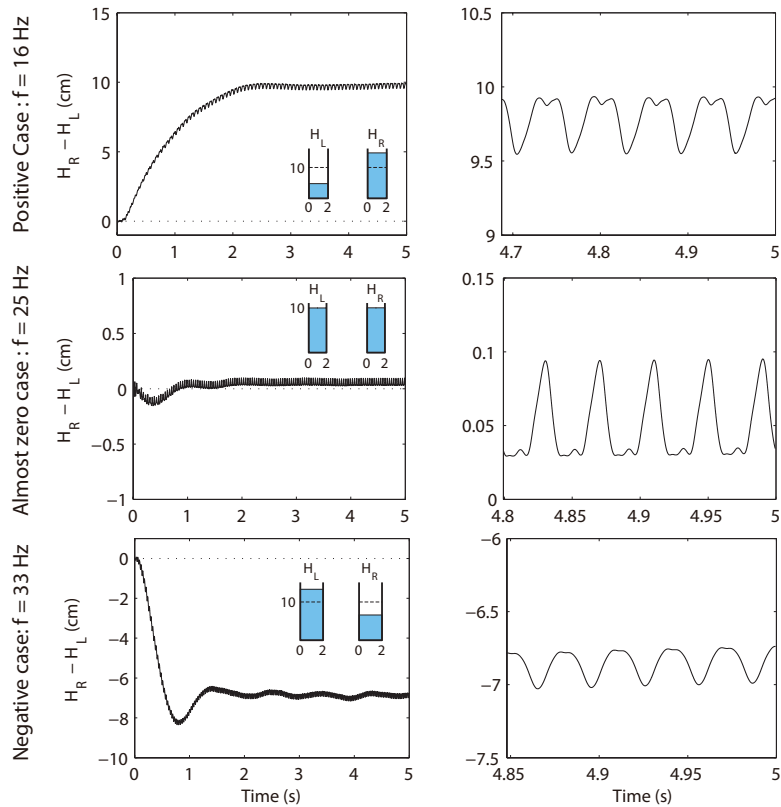duration of $5\ s$.

FIGURE 9. Case studies: the left column shows the height difference between two tanks as a function of time over the simulation time of $5\,s$, and the right column shows the motions of the height difference $H_R$-$H_L$ during the last five cycles in detail.

Figs. 11 and 12 show six snapshots of the tube boundaries and fluid motions over one period for the case of positive ($f = 16\,Hz$) and negative ($f = 33\,Hz$) net directional flows, respectively. One period for the snapshots is chosen during the transition time starting at $5\ s$. The first snapshot is chosen at $t = 0.5\,s$, which is during the transition time before the steady state is reached (see Fig. 9). The tail represents the trace of the fluid marker, and the red wall boundary represents the region for periodic pumping. The fluid levels in the virtual tanks are shown in each snapshot. For a positive net directional flow (Fig. 11), the fluid motions are driven by the compression period and the release period in the top three frames and the bottom three frames, respectively. For
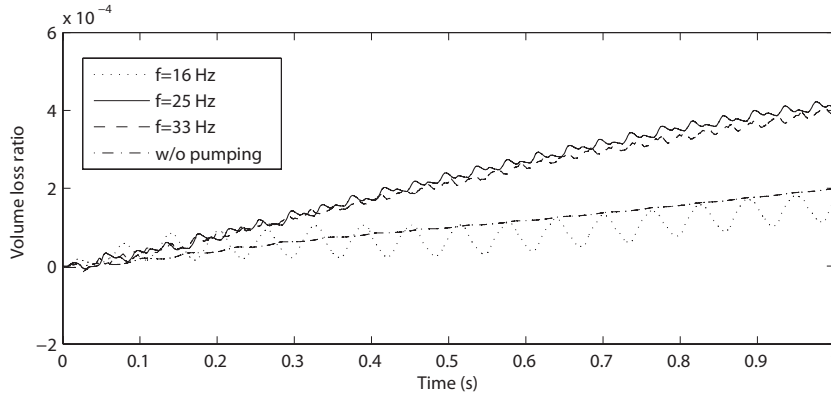
FIGURE 10. The volume loss ratios, $(V_{ini} - V(t))/V_{ini}$, are shown for different cases with $f = 16\,Hz$ (dot), $25\,Hz$ (solid), and $33\,Hz$ (dash) and without pumping (dotted dash) as a function of time.

a negative net directional flow (Fig. 12), the release period is shown in the top three frames and the compression period is shown in the bottom three frames.

In Fig. 13, the top and bottom frames show five flow-pressure loops over one period for a positive ($f = 16\,Hz$) and negative net directional flow ($f = 33\,Hz$), respectively. The space-averaged flows (Q) and pressures (P) are measured at five equispaced locations along the elastic tube at $t = 0.5\,s$, which is during the transition time before the steady state is reached (see Fig. 9). The red and blue colors indicate positive and negative flows, respectively. The black arrow indicates the starting point and direction of the PQ loop. We defined the signed area in [17] as the area difference between the positive flow (red) and the negative flow (blue). In the flow-pressure loops at five cross sections in the top frame of Fig. 13, the sum of the areas surrounded by positive flow (red) is greater than that of areas surrounded by negative flow (blue). The net flows and space-averaged signed areas along the tube for positive and negative directional flows are shown in Table 3. This result shows that the sign of the net directional flow is the same as that of the signed area, and the magnitude of the net directional flow is explained by the amount of net power over one cycle (rate of energy change along the tube over one cycle). This result is consistent with the result from the open tube system of the VP [17].

## 5. Summary and conclusions

We have developed a multidimensional model of an open VP system that consists of an elastic tube connected with two tanks. The elastic tube model is governed by a two-dimensional full Navier-Stokes system, whereas the system
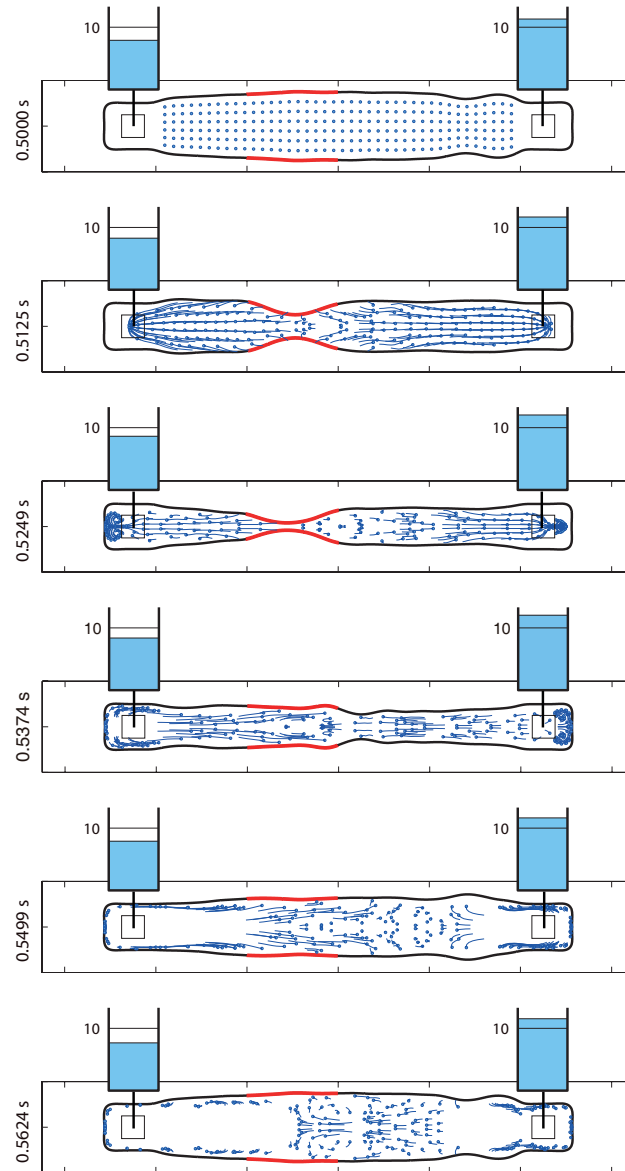
FIGURE 11. Positive net directional flow ($f = 16\,Hz$): six snapshots of the tube boundaries and fluid motions are shown. The fluid levels in the virtual tanks are shown in each snapshot. The rectangular box including the elastic tube is a magnified view and is not the exact size of the computational box.

FIGURE 12. Negative net directional flow ($f = 33\,Hz$): six snapshots of the tube boundaries and fluid motions are shown. The fluid levels in the virtual tanks are shown in each snapshot. The rectangular box including the elastic tube is a magnified view and is not the exact size of the computational box.
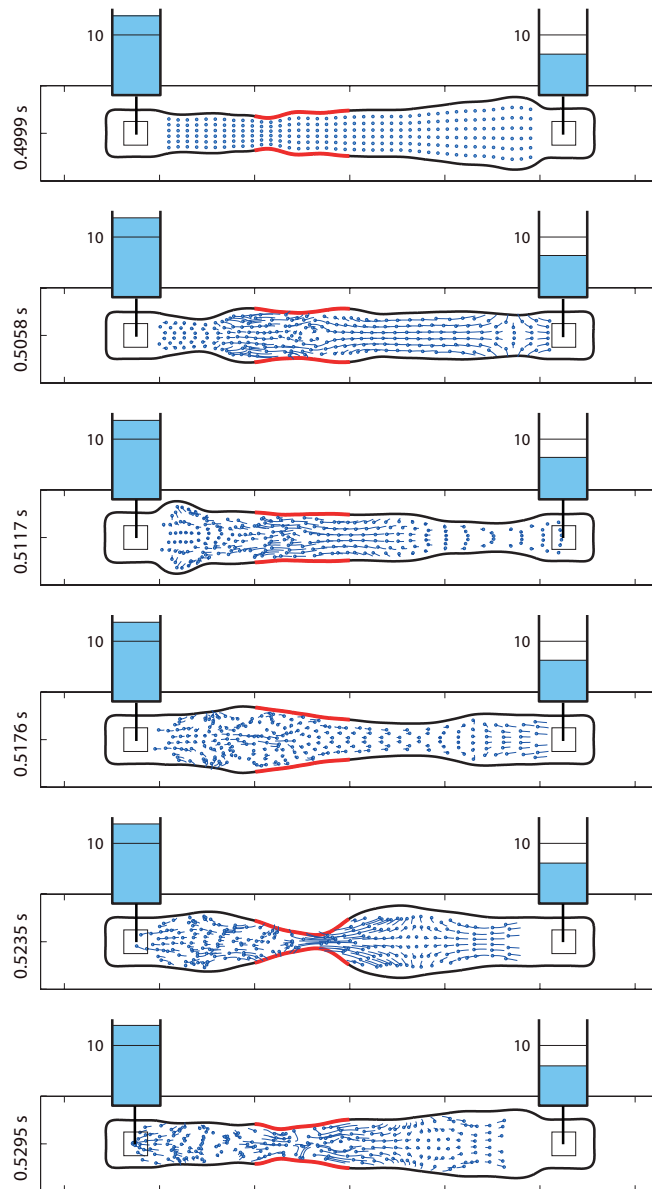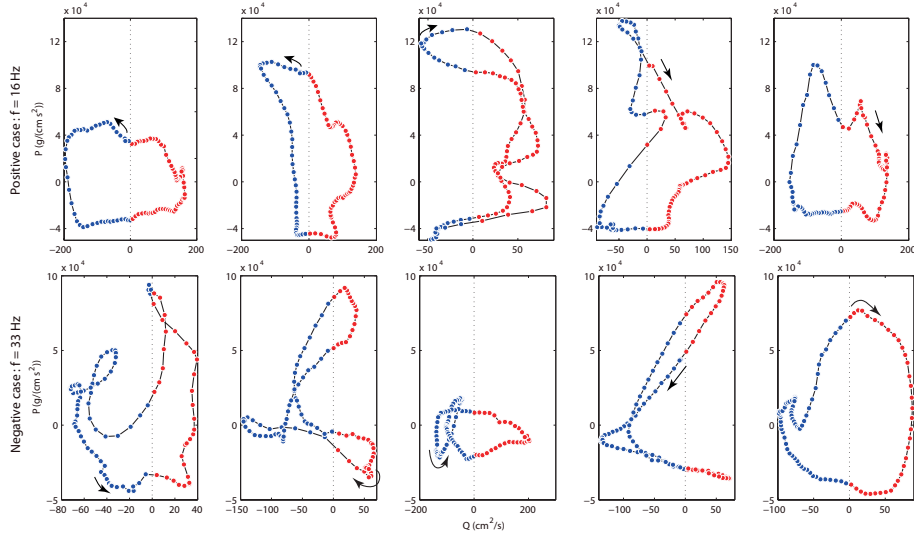
FIGURE 13. The five pressure-flow loops over one period at $t = 0.5\,s$ for a positive $(f = 16\,Hz)$ and negative $(f = 33\,Hz)$ net directional flow are shown in the top and bottom frame, respectively. From the transient time $0.5\,s$, 100 points over one pumping cycle are shown. The red points indicate positive flux and the blue points, negative flux. The black arrow indicates the direction of the loop at the starting point.

TABLE 3. The height difference and the net signed area

| Frequency | $H_R - H_L$ | Net signed area |
|---|---|---|
| $f = 16\,Hz$ (positive case) | $8.066\,cm$ | $8.7859 \times 10^5$ |
| $f = 33\,Hz$ (negative case) | $-6.637\,cm$ | $-3.6551 \times 10^4$ |

of ODE for the open tanks is constructed by applying the energy principle to a single fluid parcel under gravity.

A volume-conserved IB method is employed for solving the elastic tube, and the Runge-Kutta-Fehlberg method is used for solving the ODE model for tanks. We have modified the algorithm that was developed for solving the heart model in the whole circulatory system in [16]. The fluid solver is the same; the critical point is how it is combined with the ODE system. Toward this end, based on the work-energy principle under gravity, the fluid in a tank is viewed as a single parcel, and then, the resultant ODE is derived instead of using the compartment model for the closed circulatory system in [13]. Using

the pressure-flow relationship and the linearity of the discretized Navier-Stokes equations, the ODE model can successfully be merged into the PDE system.

Using the combined IB model, the relevant fluid dynamics was investigated by the oscillatory periodic compress-release actions that were applied to the second quarter of the soft part of the tube. A net directional flow is defined by a flow causing a height difference between the two tanks after the periodic steady-state is reached. This concept of net directional flow corresponds to a net flow in a closed VP system. The main feature of this study is that we can observe a net directional flow in our open VP system as observed in previous studies on closed and open VP systems. We have also shown that the pumping frequency and compression duration are important factors for determining the direction and magnitude of a net directional flow. Relatively, the large height difference between two tanks is observed near half the compression duration of pumping in our model setting. The location and width of the pumping region are also important factors in VP systems. In our simulations, four different locations of the pumping source in a fixed length are considered. The height difference between two tanks as a function of frequency is investigated at four pumping locations. This result indicates that there is no consistency among the four curves, and an efficient net directional flow can be obtained by changing the pumping location if the width of the pumping region is fixed. Next, we change the width of the pumping region with a fixed center of pumping. We showed that the peaks of the height difference between the two tanks are maintained at similar frequencies, although the pumping width changes. The longer the pumping width, the larger is the obtained net directional flow. To investigate the flow configuration and wall motions of the elastic tube in detail, the following three cases are chosen: a positive peak ($f = 16\,Hz$), an almost zero ($f = 25\,Hz$), and a negative peak ($f = 33\,Hz$) net directional flow from among the results shown in Fig. 4. Almost periodic oscillatory motions having level differences are observed in all three cases. and tube wall including the height differences in the two tanks.

To the best of our knowledge, ours is the first study to simulate a multidimensional model in an open tank VP system. We can extend this model to ones with more tanks to investigate the effect of the number of tanks or the size of tanks on the VP system. We can also extend our model to a three and zero-dimensional multiscale model, in order to investigate realistic phenomena of the fluid-structure interaction. Our developed algorithm can be applied to other problems including the fluid-structure interaction model with either a closed or an open ODE system.

## References

[1] D. Auerbach, W. Moehring, and M. Moser, *An analytic approach to the liebau problem of valveless pumping*, Cardiovascular Engineering: An International Journal **4** (2004), no. 2, 201–207.

[2] R. P. Beyer, *A computational model of the cochlea using the immersed boundary method*, J. Comput. Phys. **98** (1992), no. 1, 145–162.

[3] A. Borzi and G. Propst, *Numerical investigation of the liebau phenomenon*, Z. Angew. Math. Phys. **54** (2003), no. 6, 1050–1072.

[4] T. T. Bringley, S. Childress, N. Vandenberghe, and J. Zhang, *An experimental investigation and a simple model of a valveless pump*, Phys. Fluids **20** (2008), no. 3, 033602; http://dx.doi.org/10.1063/1.2890790

[5] L. J. Fauci, *Peristaltic pumping of solid particles*, Comput. Fluids **21** (1992), no. 4, 583–598.

[6] L. J. Fauci and C. S. Peskin, *A computational model of aquatic animal locomotion*, J. Comput. Phys. **77** (1988), no. 1, 85–108.

[7] A. L. Fogelson and C. S. Peskin, *A fast numerical method for solving the three-dimensional stokes' equations in the presence of suspended particles*, J. Comput. Phys. **79** (1988), no. 1, 50–69.

[8] S. Greenberg, D. M. McQueen, and C. S. Peskin, *Three-dimensional fluid dynamics in a two-dimensional amount of central memory*, Wave motion: theory, modelling, and computation (Berkeley, Calif., 1986), 85–146, Math. Sci. Res. Inst. Publ., 7, Springer, New York, 1987.

[9] B. E. Griffith and C. S. Peskin, *On the order of accuracy of the immersed boundary method: higher order convergence rates for sufficiently smooth problems*, J. Comput. Phys. **208** (2005), no. 1, 75–105.

[10] A. I. Hickerson and M. Gharib, *On the resonance of a pliant tube as a mechanism for valveless pumping*, J. Fluid Mech. **555** (2006), 141–148.

[11] E. Jung, *2-D simulations of valveless pumping using the immersed boundary method*, PhD thesis, New York University, Graduate School of Arts and Science, 1999.

[12] E. Jung, *A mathematical model of valveless pumping: A lumped model with time-dependent compliance, resistance, and inertia*, Bull. Math. Biol. **69** (2007), no. 7, 2181–2198.

[13] E. Jung and W. Lee, *Lumped parameter models of cardiovascular circulation in normal and arrhythmia cases*, J. Korean Math. Soc **43** (2006), no. 4, 885–897.

[14] E. Jung, S. Lim, W. Lee, and S. Lee, *Computational models of valveless pumping using the immersed boundary method*, Comput. Methods Appl. Mech. Engrg. **197** (2008), no. 25-28, 2329–2339.

[15] E. Jung and C. S. Peskin, *Two-dimensional simulations of valveless pumping using the immersed boundary method*, SIAM J. Sci. Comput. **23** (2001), no. 1, 19–45.

[16] Y. Kim, W. Lee, and E. Jung, *An immersed boundary heart model coupled with a multicompartment lumped model of the circulatory system*, SIAM J. Sci. Comput. **32** (2010), no. 4, 1809–1831.

[17] W. Lee, E. Jung, and S. Lee, *Simulations of valveless pumping in an open elastic tube*, SIAM J. Sci. Comput. **31** (2009), no. 3, 1901–1925.

[18] W. Lee, S. Lim, and E. Jung, *Dynamical motion driven by periodic forcing on an open elastic tube in fluid*, Commun. Comput. Phys. **12** (2012), no. 2, 494–514.

[19] G. Liebau, *Über ein ventilloses pumpprinzip*, Naturwissenschaften **41** (1954), 327–327.

[20] G. Liebau, *Die stromungsprinzipien des herzens*, Z. Kreislaufforsch **44** (1955), 677–684.

[21] G. Liebau, *Die bedeutung der tragheitskrafte fur die dynamik des blutkreislaufs*, Z. Kreislaufforsch **46** (1957), 428–438.

[22] S. Lim and E. Jung, *Three-dimensional simulations of a closed valveless pump system immersed in a viscous fluid*, SIAM J. Appl. Math. **70** (2010), no. 6, 1999–2022.

[23] S. Lim and C. S. Peskin, *Simulations of the whirling instability by the immersed boundary method*, SIAM J. Sci. Comput. **25** (2004), no. 6, 2066–2083.

[24] C. G. Manopoulos, D. S. Mathioulakis, and S. G. Tsangaris, *One-dimensional model of valveless pumping in a closed loop and a numerical solution*, Phys. Fluids **18** (2006), 017106.

[25] D. M. McQueen, C. S. Peskin, and E. L. Yellin, *Fluid dynamics of the mitral valve: physiological aspects of a mathematical model*, Am. J. Physiol. Heart Circ. Physiol. **242** (1982), H1095–H1110.

[26] J. T. Ottesen, *Valveless pumping in a fluid-filled closed elastic tube-system: one-dimensional theory with experimental validation*, J. Math. Biol. **46** (2003), no. 4, 309–332.

[27] C. S. Peskin, *Flow patterns around heart valves*: *a digital computer method for solving the equations of motion*, PhD thesis, Sue Golding Graduate Division of Medical Sciences, Albert Einstein College of Medicine, Yeshiva University, 1972.

[28] C. S. Peskin, *Numerical analysis of blood flow in the heart*, J. Comput. Phys. **25** (1977), no. 3, 220–252.

[29] C. S. Peskin and D. M. McQueen, *A three-dimensional computational method for blood flow in the heart I. Immersed elastic fibers in a viscous incompressible fluid*, J. Comput. Phys. **81** (1989), no. 2, 372–405.

[30] C. S. Peskin and D. M. McQueen, *A general method for the computer simulation of biological systems interacting with fluids*, Sympos. Soc. Exp. Biol. **49** (1995), 265–276.

[31] C. S. Peskin and B. F. Printz, *Improved volume conservation in the computation of flows with immersed elastic boundaries*, J. Comput. Phys. **105** (1993), no. 1, 33–46.

[32] G. Propst, *Pumping effects in models of periodically forced flow configurations*, Phys. D **217** (2006), no. 2, 193–201.

[33] K. A. Rejniak, *A single-cell approach in modeling the dynamics of tumor microregions*, Math. Biosci. Eng. **2** (2005), no. 3, 643–655.

[34] D. Rinderknecht, A. I. Hickerson, and M. Gharib, *A valveless micro impedance pump driven by electromagnetic actuation*, J. Micromech. Microeng. **15** (2005), 861–866.

[35] S. J. Shin and H. J. Sung, *Three-dimensional simulation of a valveless pump*, Int. J. Heat Fluid Flow **31** (2010), no. 5, 942–951.

[36] H. Thomann, *A simple pumping mechanism in a valveless tube*, Z. Angew. Math. Phys. **29** (1978), no. 2, 169–177.

[37] S. Timmermann and J. T. Ottesen, *Novel characteristics of valveless pumping*, Phys. Fluids **21** (2009), 053601.

EUNOK JUNG
DEPARTMENT OF MATHEMATICS
KONKUK UNIVERSITY
SEOUL 143-701, KOREA
*E-mail address*: junge@konkuk.ac.kr

DO WAN KIM
DEPARTMENT OF MATHEMATICS
INHA UNIVERSITY
INCHEON 402-751, KOREA
*E-mail address*: dokim@inha.ac.kr

JONGGUL LEE
DEPARTMENT OF MATHEMATICS
KONKUK UNIVERSITY
SEOUL 143-701, KOREA
*E-mail address*: jack9872@konkuk.ac.kr

Wanho Lee
National Institute for Mathematical Sciences
Daejeon 305-811, Korea
*E-mail address*: wlee@nims.re.kr